

VELOCITY ANISOTROPY IN SELF-GRAVITATING MOLECULAR CLOUDS. I: SIMULATION

FRANK OTTO

Department of Physics, The Chinese University of Hong Kong

WEIGUANG JI

Xinjiang Astronomical Observatory, Urumqi, Xinjiang, China
and

Department of Physics, The Chinese University of Hong Kong

HUA-BAI LI

Department of Physics, The Chinese University of Hong Kong

ABSTRACT

The complex interplay between turbulence, magnetic fields, and self-gravity leads to the formation of molecular clouds out of the diffuse interstellar medium (ISM). One avenue of studying this interplay is by analyzing statistical features derived from observations, where the interpretation of these features is greatly facilitated by comparisons with numerical simulations. Here we focus on the statistical anisotropy present in synthetic maps of velocity centroid data, which we derive from three-dimensional magnetohydrodynamic simulations of a turbulent, magnetized, self-gravitating patch of ISM. We study how the orientation and magnitude of the velocity anisotropy correlate with the magnetic field and with the structures generated by gravitational collapse. Motivated by recent observational constraints, our simulations focus on the supersonic (sonic Mach number $\mathcal{M} \approx 2 - 17$) but sub- to trans-alfvénic (alfvénic Mach number $\mathcal{M}_A \approx 0.2 - 1.2$) turbulence regime, and we consider clouds which are barely to mildly magnetically supercritical (mass-to-flux ratio equal to once or twice the critical value). Additionally we explore the impact of the turbulence driving mechanism (solenoidal or compressive) on the velocity anisotropy. While we confirm previous findings that the velocity anisotropy generally aligns well with the plane-of-sky magnetic field, our inclusion of the effects of self-gravity reveals that in regions of higher column density, the velocity anisotropy may be destroyed or even reoriented to align with the gravitationally formed structures. We provide evidence that this effect is *not* necessarily due to the increase of \mathcal{M}_A inside the high-density regions.

1. INTRODUCTION

It is commonly accepted that the interstellar medium (ISM) is governed by the competition between the forces of gravity, turbulence, and magnetic fields. The balance between these forces plays a major role e.g. for the for-

mation of molecular clouds and of stars (see e.g. [McKee & Ostriker \(2007\)](#)). Turbulence is perhaps the most elusive of these forces, because its driving mechanisms are still not well understood, it is difficult to treat theoretically, and studying it observationally requires gathering data from a large range of scales.

Due to the stochastic nature of turbulence, statistical methods are widely used to study its properties. Many of these methods work with velocity data, because spec-

frank.otto@cuhk.edu.hk

hbli@phy.cuhk.edu.hk

troscopic observations are able to provide such data in plenty, and because active turbulence will have a direct imprint on the velocity field, in contrast to the density field which may instead be imprinted with “fossil” turbulence. Notable methods which work on position-velocity (PPV) cubes include the “spectral correlation function” (Rosolowsky et al. 1999), the “velocity channel analysis” (Lazarian & Pogosyan 2000), and the “velocity coordinate spectrum” (Lazarian 2004). A less elaborate, but still useful method, makes use of the two-point correlation functions of the velocity centroid (Esquivel et al. 2003; Esquivel & Lazarian 2005, 2011; Burkhart et al. 2014), and we also employ this method in the present work.

While astrophysical turbulence is often assumed to be driven in an isotropic manner, the presence of magnetic fields introduces anisotropic behavior, because charged particles are forced to circulate around the magnetic field lines while they may move freely along them. The size of this effect depends on scale. While large-scale turbulent motions contain more kinetic energy than small-scale motions, the local magnetic field strength and hence the magnetic energy density are roughly independent of scale. Therefore the magnetic influence is more pronounced on small scales, and leads to elongation of the turbulent eddies. A theoretical model for magnetohydrodynamic (MHD) turbulence in incompressible media was presented by Goldreich & Sridhar (1995, hereafter GS95), and its predictions for the anisotropic scaling behavior of power spectra have been confirmed by numerical simulations (Cho & Vishniac 2000; Cho et al. 2002), and have been found to also apply for compressible media (Cho & Lazarian 2003), thus showing its relevance for studies of the ISM.

Studying this magnetically induced anisotropy from (synthetic) observations of velocity data has been the topic of a series of studies (Esquivel & Lazarian 2011; Burkhart et al. 2014; Esquivel et al. 2015) based on numerical simulations of MHD turbulence. It was found that the anisotropy can be reliably detected and used to recover the mean orientation of the plane-of-sky (POS) component of the magnetic field (B -field) for sub- to slightly super-alfvénic conditions ($\mathcal{M}_A \lesssim 1.5$), and even if the B -field is moderately inclined ($< 40^\circ$) with respect to the POS. On the observational side, Heyer et al. (2008) applied a directional variant of principal component analysis to a ^{12}CO PPV cube from the Taurus molecular cloud, and found a significant correlation between the velocity anisotropy and the mean POS B -field orientation. In a followup study (Heyer & Brunt 2012), no such anisotropy was found in the ^{13}CO data which trace the high-density, filamentary region of the

cloud. This difference was attributed to the transition from sub- to super-alfvénic turbulence between the low- and high-density regions.

However, magnetic fields are not the only possible source for velocity anisotropy. Self-gravity in molecular clouds leads eventually to the formation of large-scale structures, which are often found to be filamentary, and these oriented structures can have an imprint on the velocity field of the surrounding medium. To our knowledge, the effect of self-gravity on the turbulent velocity anisotropy has not been investigated.

In this study, we present the results from a series of numerical simulations of driven magnetohydrodynamic turbulence including self-gravity. Our simulations focus on sub- to trans-alfvénic conditions, i.e. where the magnetic field dominates over or competes with the turbulence. This choice is motivated by recent observational constraints (Li et al. 2009, 2013, 2014, 2015a) which indicate that the magnetic field is ordered over a large range of scales, a scenario which is difficult to reconcile with dominating turbulence as this should lead to rather tangled magnetic field structures. While many numerical simulations in the past have favored such super-alfvénic scenarios, recent simulations have also started to explore the sub- to trans-alfvénic regime (e.g. Li et al. (2015b)).

In addition to a range of sonic and alfvénic Mach numbers ($\mathcal{M}_{\text{sonic}} = 1.8 - 17.3$ and $\mathcal{M}_{\text{alfvén}} = 0.2 - 1.2$), we explore two different scenarios for the relative strength between gravity and magnetic forces: one where the simulated volume as a whole is in equilibrium between these forces, and one where the cloud mass is twice the magnetically critical mass. Again, the choice for these parameters is motivated from recent observational constraints (Li et al. 2015a). Additionally we investigate whether the turbulence driving mechanism, which may be of more solenoidal or more compressive nature (Federrath et al. 2010), has an influence on the velocity anisotropy.

Our simulation methodology is detailed in Section 2. From our simulations, we produce synthetic maps of the line-of-sight (LOS) velocity centroid, and we employ a novel method to detect and quantify the velocity anisotropy from these maps. (Section 3). We then investigate if and how the anisotropy correlates with the B -field orientation and with the gravitationally formed structures. (Section 4). A discussion and comparison with previous related results is provided in Section 5.

2. SIMULATION METHOD

ID	B_0	\dot{e}_{drv}	solenoidal ($\zeta 1$)				compressive ($\zeta 0$)			
			\mathcal{M}	\mathcal{M}_A	AR1	AR2	\mathcal{M}	\mathcal{M}_A	AR1	AR2
B0E1	0	10	2.01	∞	–	–	1.90	∞	–	–
B0E3	0	1000	8.67	∞	–	–	8.65	∞	–	–
B3E1	3	10	1.89	0.63	4.5	8.4	1.79	0.60	5.6	7.1
B3E2	3	100	3.71	1.24	3.7	4.4	3.58	1.19	4.9	3.3
B10E1	10	10	2.37	0.24	10.0	5.6	2.01	0.20	10.2	2.0
B10E2	10	100	4.06	0.41	7.8	2.7	3.73	0.37	9.8	3.9
B10E3	10	1000	8.20	0.82	3.1	4.6	7.87	0.79	3.1	1.9
B30E3	30	1000	9.11	0.30	3.6	2.8	8.42	0.28	4.3	4.0
B30E4	30	10000	17.3	0.57	2.8	2.8	N/A	N/A	–	–

Table 1. List of simulations and parameters used. B_0 and \dot{e}_{drv} are input parameters (see text). The sonic and alfvénic Mach numbers derive from the velocity dispersion v_{rms} , which for each simulation is calculated by averaging over a series of snapshots of fully developed turbulence. The spread of v_{rms} yields an estimate for the relative uncertainty of \mathcal{M} and \mathcal{M}_A of about 5% (at 95% confidence level). The AR columns list the maximum aspect ratio of the top-10% autocorrelation contour of the column density as encountered during the gravitational stage of the simulations, AR1 for $cr = 1$ and AR2 for $cr = 2$; see Section 4.3.

We perform a set of three-dimensional ideal magnetohydrodynamics (MHD) simulations, using a modified version of the code ZEUS-MP (Hayes et al. 2006). The major modification is an implementation of the turbulence driving scheme described in (Stone et al. 1998). While this scheme originally only used solenoidal (non-compressive) driving modes, we extend it to allow for an arbitrary mix of solenoidal and compressive modes, following (Schmidt et al. 2006). For completeness, mathematical details of our driving scheme are given in Appendix A.

Starting from uniform initial conditions, our simulations proceed in two stages. In the first stage, self-gravity is turned off, and turbulence is driven until the turbulent cascade is saturated (or longer). This is judged by verifying that the power spectrum of the kinetic energy has reached a stable distribution. In the second stage, self-gravity is turned on, while turbulence driving continues. The gravitational stage is run for several free-fall times, if possible, though in the more supercritical scenarios the gravitational collapse can quickly lead to very high densities, which causes very small MHD time steps and forces a stop of the simulation. All the simulations use an isothermal equation of state, and periodic boundary conditions are employed.

The output of each simulation is a series of snapshot datacubes, each containing the mass density $\rho(\mathbf{x}, t)$, the velocity field $\mathbf{v}(\mathbf{x}, t)$, and the magnetic field vector $\mathbf{B}(\mathbf{x}, t)$, on a uniform 3D grid of N^3 points \mathbf{x} , at a specific simulation time t . Our simulations are resolved with $N = 576$ points per dimension.

The simulations are carried out in reduced units, such that the average mass density ρ_0 , the isothermal sound speed c_s , and the box length L have unit value. Turbu-

lence is driven at large wavelengths ($L_{\text{drv}} = 0.5L$), and its strength is controlled by the specific kinetic energy input rate \dot{e}_{drv} (measured in units of c_s^2). The magnetic field, if present, is initially uniform, with strength B_0 (in units such that the magnetic pressure is given by $\mathbf{B}^2/2$) and pointing in the z -direction. These two parameters, \dot{e}_{drv} and B_0 , determine the root-mean-square velocity dispersion $v_{\text{rms}} = \langle [\mathbf{v}(\mathbf{x}) - \langle \mathbf{v}(\mathbf{x}) \rangle_{\mathbf{x}}]^2 \rangle_{\mathbf{x}}^{1/2}$ (where $\langle \rangle_{\mathbf{x}}$ denotes the spatial average), and hence set the turbulent sonic Mach number $\mathcal{M} = v_{\text{rms}}/c_s$, as well as the Alfvén Mach number $\mathcal{M}_A = v_{\text{rms}}/v_A$, where $v_A = B_0/\sqrt{\rho_0}$ is the large-scale Alfvén speed. To investigate the influence of the turbulence driving mode, we have carried out simulations both with purely solenoidal driving ($\zeta = 1.0$; see Appendix A) and with purely compressive driving ($\zeta = 0.0$). Table 1 lists the simulation parameters which have been used for the present work. All our simulations are supersonic, and most of them are sub-alfvénic. In the following, we will refer to the simulations by their ID, appended with “ $\zeta 1$ ” or “ $\zeta 0$ ” for indicating whether solenoidal or compressive driving is used, respectively.

For the gravitational stage, we additionally use the gravitational constant G as a parameter to control the relative strength between gravity and magnetic forces. The latter stabilize the cloud against collapse if the total cloud mass $M = \rho_0 L^3$ is less than $M_{\Phi} = f\Phi\sqrt{4\pi/G}$, where $\Phi = B_0 L^2$ is the magnetic flux through the cloud, and f is a geometric factor for which we use the value $f = 1/2\pi$ (Nakano & Nakamura 1978). Hence the *criticality* parameter $cr = M/M_{\Phi}$ controls how (magnetically) supercritical the cloud is, as a whole. For this work, we have carried out the gravitational stage of the simulations with both $cr = 1$ and $cr = 2$.

An example for how our reduced units can be converted

to physical units will be given in Section 5.

3. ANALYSIS METHOD

3.1. Detecting anisotropy strength and orientation

Our analysis focuses on the velocity centroid, as this is a quantity which is readily available from observed spectroscopic data. It is also readily obtained from simulation data as follows: for each point \mathbf{r} on the plane-of-sky, the velocity centroid $V(\mathbf{r})$ is computed by integrating the line-of-sight velocity component v_{LOS} along the line-of-sight coordinate s , weighted with the local emission intensity, and normalized by the total emission intensity. Under optically thin assumptions, the local emission intensity is proportional to the local gas density ρ , so that

$$V(\mathbf{r}) = \frac{\int ds \rho(\mathbf{r}, s) v_{\text{LOS}}(\mathbf{r}, s)}{\int ds \rho(\mathbf{r}, s)}. \quad (1)$$

To identify stochastic anisotropies in this 2D map of velocity centroids, following Esquivel & Lazarian (2011), we look at its two-point second order structure function, which is given by averaging the squared difference in the velocity centroid between any two points on the map which are separated by the distance vector \mathbf{l} :

$$SF_V(\mathbf{l}) = \left\langle [V(\mathbf{r}) - V(\mathbf{r} + \mathbf{l})]^2 \right\rangle_{\mathbf{r}} \quad (2)$$

This structure function depends on the distance l separating the point pairs, and on the plane-of-sky (POS) angle φ (measured counter-clockwise from the POS horizontal axis),

$$SF_V(l, \varphi) = SF_V(l \hat{\mathbf{e}}_\varphi)$$

where $\hat{\mathbf{e}}_\varphi$ is a unit vector with POS angle φ .

When evaluating Eq. (2) for a given distance vector \mathbf{l} in practice, the average is computed by running over all grid points \mathbf{r} of the 2D map, provided that $\mathbf{r} + \mathbf{l}$ is also within the map. Moreover, if \mathbf{l} is not aligned with one of the grid axes, the point $\mathbf{r} + \mathbf{l}$ will in general not fall onto a grid point, so that the corresponding velocity centroid value $V(\mathbf{r} + \mathbf{l})$ is not directly available from Eq. (1); instead, we compute it by bilinear interpolation from the velocity centroid on the four neighboring grid points.

To measure the anisotropy present in the structure function SF_V , we fit (least-squares minimization) its angular behaviour to the following model function:

$$SF_V(l, \varphi) \sim c_l [1 - b_l \cos(2(\varphi - \alpha_l))] \quad (3)$$

This fit is done for each scale l , and yields a measure of the *anisotropy strength* b_l and of the *anisotropy orienta-*

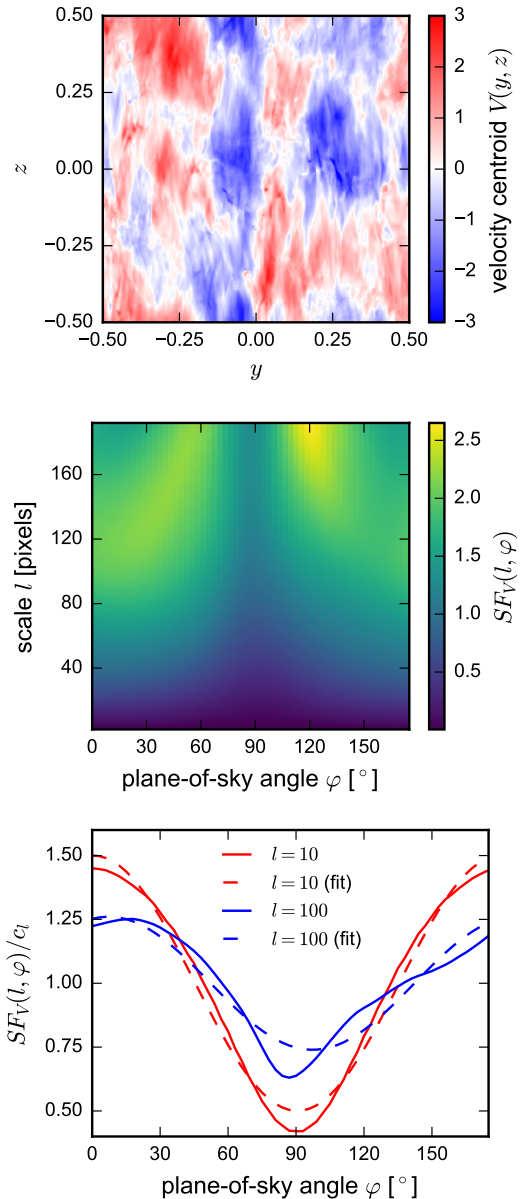


Figure 1. (Color online.) *Top:* Map of the velocity centroid $V(\mathbf{r})$ with line of sight along the x -direction (snapshot from the B10E2 ζ 1 simulation, with saturated turbulence, no gravity). The mean magnetic field points upwards. *Middle:* Map of the structure function SF_V as a function of scale l and POS angle φ . At all scales, the structure function exhibits a minimum around $\varphi = 90^\circ$, the direction parallel to the magnetic field. *Bottom:* Normalized structure function $SF_V(l, \varphi)/c_l$ plotted against the plane-of-sky angle φ . Solid lines show the actual data for the scales $l = 10$ px (red color) and $l = 100$ px (blue color), while the dotted lines show the corresponding fits according to the model function Eq. (3).

tion α_l . We restrict $b_l \geq 0$ and $0 \leq \alpha_l < 180^\circ$ to enforce a unique solution. The coefficient $c_l = \langle SF_V(l, \varphi) \rangle_\varphi$ measures the average structure function at scale l , and plays no role in determining the anisotropy.

Fig. 1 illustrates our procedure for obtaining the

anisotropy strength and orientation, using one snapshot of the sub-alfvénic simulation B10E2 ζ 1. While the plane-of-sky map of the velocity centroid (top panel) exhibits anisotropy which can be visually recognized, the picture becomes much clearer when looking at how the structure function SF_V depends on the scale l and the POS angle φ (middle panel). At all scales, SF_V exhibits a minimum where the POS angle aligns with the mean POS B -field orientation (here, $\varphi \approx 90^\circ$). When looking at the detailed angular dependence for a single scale (bottom panel), the approximately sinusoidal angle-dependence of SF_V becomes apparent, and the position of the fitted sinusoid’s minimum informs us about the anisotropy’s orientation (α_l) while the fitted sinusoid’s amplitude yields a measure for the anisotropy’s strength (b_l).

3.2. Parameter uncertainties

The fitting procedure described above yields, for each scale l , one value for each of the parameters α_l and b_l . However, the stochastic nature of the turbulence driving leads to fluctuations of these parameters from snapshot to snapshot. Even if the structure function is obtained by averaging over a whole snapshot, there is not enough data in a single snapshot to completely average out these fluctuations. Therefore it is essential to obtain an error estimate for the fitted parameters. We propose two methods to do so.

The first method can be applied if snapshots with equivalent physical conditions, but different realizations of the turbulent field are available. This is the case for the first stage of our simulations (i.e. before gravity is switched on): after the turbulent cascade has saturated, snapshots which are far enough separated in time are statistically independent, but correspond to equivalent physical conditions. Hence we can collect a sample of the parameters α_l and b_l from individually fitting each snapshot. This sample is then summarized by the mean anisotropy strength \bar{b}_l and mean anisotropy orientation $\bar{\alpha}_l$, and the corresponding sample standard deviations are used as error estimates. (Note that for the orientation, which is defined on a periodic interval with a period of 180° , we are using the *circular mean* and *circular standard deviation*.) Additionally, the sample size can be doubled by combining equivalent lines of sight, namely those perpendicular to the mean B -field. We will refer to these error estimates as *snapshot-sampled* errors.

The second method is designed to be used on a single snapshot. For the second stage of our simulations, which includes self-gravity, the molecular cloud can col-

lapse, and physical conditions differ between different stages of the collapse. Hence it is mandatory to estimate the errors for α_l and b_l from a single snapshot. Moreover, we are interested in analyzing not only the full POS map, but also selected subregions of it (e.g. selected by a column density threshold). This is simply achieved by including only point pairs from the selected region in the computation of Eq. (2). To obtain an error estimate for these cases, we randomly cut out from the selected region (or whole map) a set of non-overlapping disc-shaped areas (of a certain diameter D), until no further such area can be cut out; Each such disc is required to lie contiguously inside the selected region. For each disc, we then compute the structure function SF_V using only points inside the disc, and obtain the anisotropy parameters by fitting as above, yielding values $\alpha_{l,i}$ and $b_{l,i}$ for the i -th disc. These values can be regarded as points $(b_{l,i} \cos(2\alpha_{l,i}), b_{l,i} \sin(2\alpha_{l,i}))$ in a 2D plane, and the geometric center of these points defines the average anisotropy strength b_l and the average anisotropy orientation α_l . Note that the process of covering the map with non-overlapping discs doesn’t cover the whole map. Therefore it can be repeated several times, and each time a different random subregion of the map will be covered. For each covering, we obtain different values of b_l and α_l , and again these can be summarized by the means and the standard deviations. We will refer to the error estimates obtained in this way as *disc-sampled* errors.

Some technical notes for the disc-sampling error estimates are in order. First, the shape of disc is chosen so as not to bias the detection of the anisotropy orientation – there is no preferred orientation in a disc. Second, the method is restricted to scales l much smaller than the disc diameter D , because for scales close to D , there is an insufficient number of point pairs to reliably compute a stochastic average of the structure function at that scale – figuratively speaking, there is only a small number of turbulent eddies at larger scales, which precludes a meaningful statistical analysis. Third, as the disc-sampling method operates on a single snapshot, it can also be applied to observational data, where one also doesn’t have the luxury of having multiple snapshots available.

4. RESULTS

4.1. Baseline turbulent anisotropy

Due to the randomness of the turbulent fluctuations, weak transient anisotropies will generally appear, even in the absence of magnetic fields or gravity. To measure

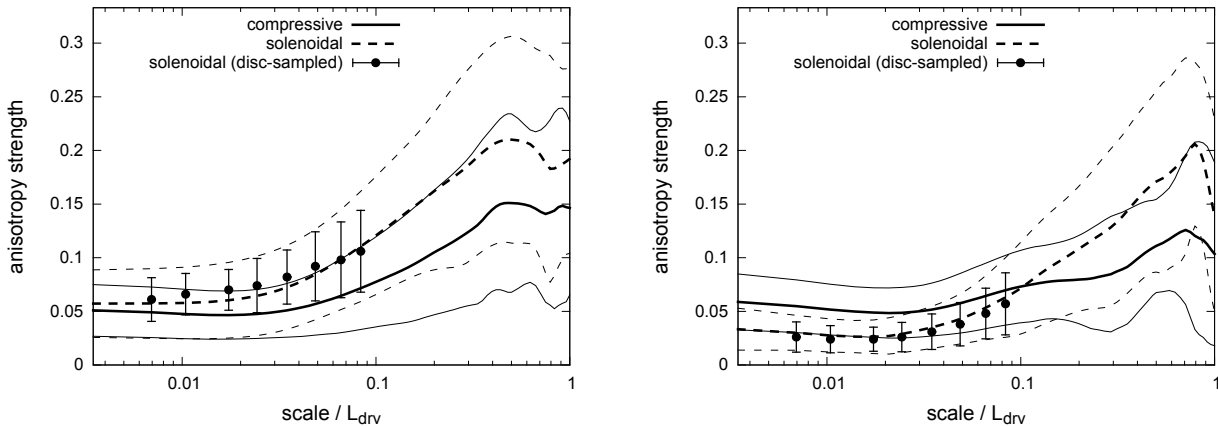


Figure 2. Scale-dependence of the anisotropy strength b for pure hydro simulations (no B -field). The left panel is for $\mathcal{M} \approx 1.95$ (B0E1) while the right panel is for $\mathcal{M} \approx 8.66$ (B0E3). Thick lines show the b data averaged over 3 lines of sight and 10 snapshots of fully developed turbulence. Thin lines indicate the corresponding 1σ deviations (snapshot-sampled). The different turbulence driving mechanisms (compressive and solenoidal) are represented by the solid and dashed lines, respectively. The individual data points show the results for solenoidal driving from a *single* snapshot (with disc-sampled errors; see text).

the anisotropy strength of these transient anisotropies, we conducted a set of pure hydrodynamic simulations (i.e. using $B_0 = 0$) and measured the anisotropy strength of the velocity centroid map as described in Section 3. Fig. 2 displays the snapshot- and LOS-averaged anisotropy strength b_l as a function of the scale l , for moderate (left panel) as well as highly (right panel) supersonic turbulence, with both compressive (solid lines) and solenoidal (dashed lines) driving. The uncertainty of the anisotropy strength has here been estimated by the snapshot-sampled errors, as described in Sec. 3.2. To verify that the disc-sampled errors give a similar estimate for the uncertainty, we have evaluated them with discs of diameter $D = 64$ px for a single snapshot, at a few scales up to $l = 24$ px. We find that the disc-sampled errors tend to be slightly smaller than the snapshot-sampled errors, though both methods agree reasonably well on the magnitude of the uncertainty.

These results set a *baseline* value for the anisotropy strength. In the following investigations, anisotropies will be considered to be non-transient (i.e. caused by other effects than random turbulent fluctuations) only if the measured anisotropy strength lies significantly above this baseline strength.

We can make the following observations: First, the strength of transient anisotropies increases with the scale l , reaching a plateau at the driving scale L_{drv} . This can be understood by noting that for larger scales, the number of turbulent eddies at that scale becomes smaller, so that the random orientations of these few eddies are less likely to average out. On the other hand, at small scales a large number of eddies is present, and averaging over them leads to a weaker residual anisotropy. Second, we don't find a conclusive influence of the turbu-

lence driving mode on the baseline anisotropy strength, as the results agree within their 1σ deviations. Third, the results differ very little between simulations with different sonic Mach number. We find the baseline anisotropy strength to generally lie between $b \approx 0.05$ at small scales and $b \lesssim 0.25$ at scales near the driving scale.

Finally, we note that the orientations of these transient anisotropies are distributed randomly, as expected in the absence of a governing direction like the magnetic field. To verify, Fig. 3 shows the distribution of the measured anisotropy orientation for one of the pure hydrodynamic simulations.

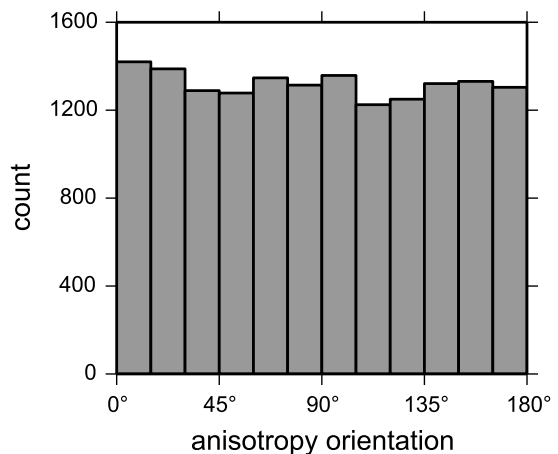


Figure 3. Distribution of the plane-of-sky angle of the velocity anisotropy at the scale $l = 24$ px, determined for the B0E1 ζ 1 simulation using disc-sampled ($D = 64$ px) data from 10 snapshots and 3 lines of sight.

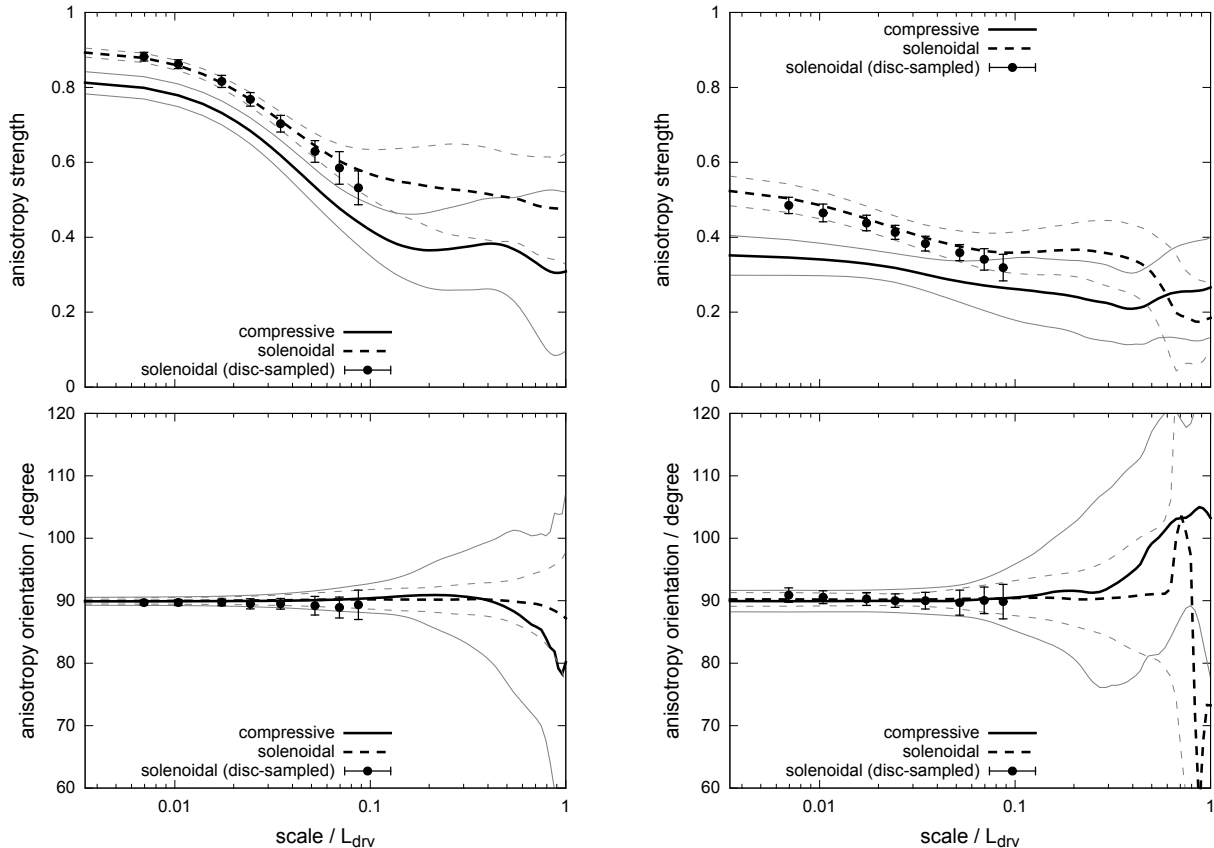


Figure 4. Scale-dependence of the anisotropy strength (top panels) and the anisotropy orientation (bottom panels) for strongly sub-alfvénic MHD simulations. On the lefthand side: $\mathcal{M} \approx 2.2$, $\mathcal{M}_A \approx 0.22$ (B10E1); on the righthand side: $\mathcal{M} \approx 8.7$, $\mathcal{M}_A \approx 0.29$ (B30E3). Thick lines show data averaged over several snapshots of fully developed turbulence, and averaged over the two lines of sight perpendicular to the mean B -field. Thin lines indicate the corresponding 1σ deviations (snapshot-sampled). Solid and dashed lines show data for compressive and solenoidal turbulence driving, respectively. As in Fig. 2, the individual data points show the results for solenoidal driving from a *single* snapshot with disc-sampled errors.

4.2. Correlation between anisotropy and B -field in absence of gravity

With non-zero B -field strength, it is expected from GS95 theory that the turbulent velocity field will exhibit anisotropy aligned with the orientation of the mean B -field. Using snapshots from our simulations where turbulence is saturated, but gravity not yet switched on, we have measured the anisotropy from the velocity centroid maps where the LOS is perpendicular to the B -field, and indeed we find that the velocity anisotropy is significantly stronger than the baseline results from the previous section, and that it aligns very well with the POS B -field orientation. On the other hand, for LOS parallel to the B -field, the velocity anisotropy shows behavior basically indistinguishable from the baseline ($B = 0$) scenario.

The velocity anisotropy is most pronounced for sub-alfvénic conditions, which is exemplified in Figure 4 with two simulations with $\mathcal{M}_A < 0.3$. In the case of mildly

supersonic turbulence (lefthand side), the anisotropy strength is very high (> 0.8) at small scales and drops continuously towards the driving scale. Likewise, the anisotropy aligns extremely well (within 1°) with the POS B -field orientation (which is at 90°) at small scales, while at larger scales the spread in the anisotropy orientation becomes more pronounced, though even at $1/4$ of the driving scale the spread is still below 10° . For strongly supersonic turbulence (righthand side), we see a similar dependence of the anisotropy strength and orientation on scale, with overall lower levels of anisotropy strength and larger spreads of orientation. Nevertheless, except for scales close to the driving scale, the anisotropy strength is significantly stronger than baseline levels, and the anisotropy aligns very well with the POS B -field, especially at small scales.

We note that the decreasing anisotropy strength and the increasing misalignment between anisotropy and B -field with increasing scale is in good agreement with the GS95 theory. As there is more kinetic energy in large-scale turbulent eddies than in small-scale ones, at large

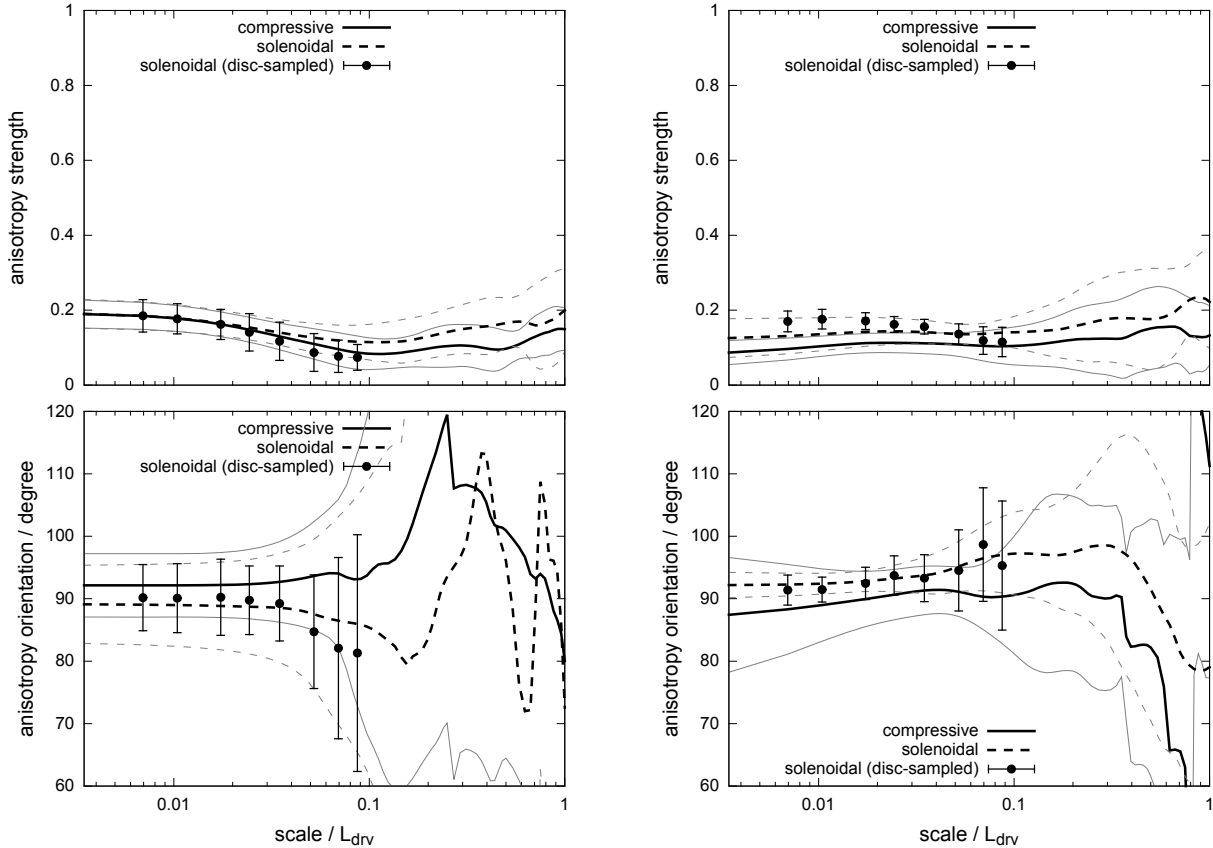


Figure 5. Like Figure 4, but for trans-alfvénic MHD simulations. Left: $\mathcal{M} \approx 3.6, \mathcal{M}_A \approx 1.2$ (B3E2). Right: $\mathcal{M} \approx 8.0, \mathcal{M}_A \approx 0.80$ (B10E3).

scales (especially close to the driving scale) turbulence will be more dominant, and skew the anisotropy results towards the baseline levels.

Figure 4 shows results both for compressive (solid lines) and solenoidal (dashed lines) turbulence driving. We observe that solenoidal driving leads to somewhat stronger anisotropies, which are also somewhat more tightly aligned with the POS B -field up to larger scales. It is possible that the more shock-like motions, which compressive driving induces, can randomly compress or elongate the turbulent eddies in random directions, thus having a disorienting effect on the overall anisotropy.

For the case of trans-alfvénic conditions ($\mathcal{M}_A \approx 1$), the scale-dependence of the strength and the orientation of the velocity anisotropy is depicted in Figure 5, with moderately supersonic conditions on the left and strongly supersonic conditions on the right. Compared to the sub-alfvénic case, the anisotropy strength is now much smaller ($b \approx 0.1 - 0.2$), but nevertheless it is still elevated compared to the baseline levels (cf. Figure 2) at small scales, where also the alignment of the anisotropy with the mean POS B -field is still good (within $\pm 10^\circ$). For larger scales though, the anisotropy

strength matches the baseline levels, and its orientation fluctuates strongly. Evidently, under these conditions, the magnetic field is only able to imprint its orientation on the velocity anisotropy at small scales, where it can dominate over turbulence.

Our results for the velocity anisotropy in the face of competition between turbulence and B -fields, but without gravity, are summarized in Figure 6. As we have seen, the anisotropy is most clearly defined at small scales; however, small scales are also strongly affected by numerical diffusion. Hence we have elected to measure it at a scale of $l = 24$ pixels $\approx 0.08 L_{\text{drv}}$. This scale is small enough to not be affected by the driving scale, it still exhibits significant anisotropy for small and medium Mach numbers, and it is big enough to avoid numerical diffusivity effects (cf. Appendix A) as well as possible orientation bias due to the discreteness of the computational grid. The figure shows, for each combination of sonic and alfvénic Mach number, the anisotropy strength measured from lines of sight perpendicular and parallel to the mean B -field. For the parallel LOS, all simulations yield a similar anisotropy strength of $b \approx 0.05$, which coincides with the baseline anisotropy strength in absence of B -fields. For the perpendicular LOS, we systemati-

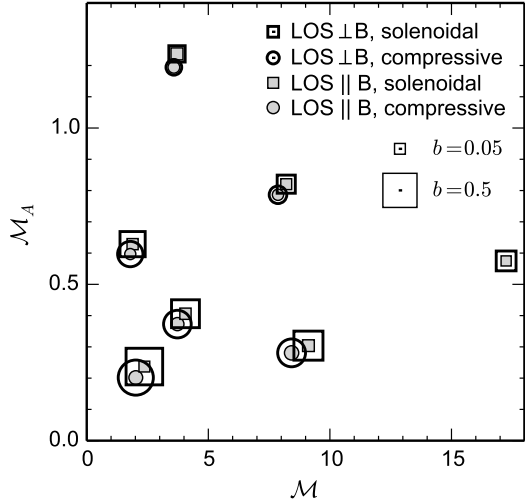


Figure 6. Anisotropy strength b as a function of sonic (\mathcal{M}) and alfvénic (\mathcal{M}_A) Mach number, for saturated turbulence. The area of each symbol is proportional to b , measured at scale $l = 24$ pixels. Open symbols show b for LOS perpendicular to the mean B -field (averaged over the two possible LOS), while the grey filled symbols show b for the LOS parallel to the B -field. Squares and circles are used to indicate solenoidal and compressive driving, respectively. Each $(\mathcal{M}, \mathcal{M}_A)$ point corresponds to one of the simulations in Table 1.

cally observe the anisotropy strength to be larger than this baseline level, most significantly so for smaller Mach numbers. Likewise, for perpendicular LOS, we note that the orientation of the anisotropy coincides very well with the POS B -field direction. The deviation is below 3° for small Mach numbers and within 20° for high Mach numbers (cf. Figures 4, 5).

4.3. Influence of gravity on velocity anisotropy

In the second stage of our simulations, we start from a snapshot with saturated turbulence and turn on gravity while the turbulence continues to be driven. The relative strength between the magnetic forces and gravity is determined by the criticality parameter cr (see Section 2), and we have run the gravitational stage of our simulations with $cr = 1$ (trans-critical cloud) and $cr = 2$ (notably supercritical cloud). We now investigate whether the oriented structures, which may form due to gravitational collapse, have an influence on the velocity anisotropy.

Figure 7 shows how the velocity anisotropy (again measured at scale $l = 24$ px) develops over time. $t = 0$ is the moment where gravity is switched on, and we normalize simulation time by the freefall time $t_{\text{ff}} = \sqrt{3\pi/32G\rho_0}$. Here we employ the disc-sampling method as described in Section 3.2, using discs of diameter $D = 64$ px, to

measure the strength and orientation of the velocity anisotropy and to estimate their uncertainties. Additionally we average over the two lines of sight perpendicular to the mean B -field, which also contributes to the uncertainty estimate. As was previously indicated in Figures 2, 4, and 5, the disc-sampled values and error estimates are in good agreement with the results from averaging over several snapshots.

The lefthand side of Figure 7 shows the B10E1 ζ 1 simulation with $cr = 1$ over a period of four freefall times. When we measure the overall velocity anisotropy for the whole map (these results are depicted by the solid lines), we note that anisotropy strength drops slightly over time (from $b \approx 0.5$ to $b \approx 0.35$) but it stays well above baseline levels. Accordingly, the anisotropy orientation maintains a very tight correlation with the POS B -field orientation. A similar behavior can be observed on the righthand side of Figure 7, which shows the results for the B3E1 ζ 0 simulation with $cr = 2$, i.e. with weaker B -field, different turbulence driving mode, and higher criticality. Here the anisotropy maintains its strength at $b \approx 0.2$, and likewise it aligns within a few degrees with the POS B -field. From these results alone, one could have the impression that gravity did not have a big influence on the simulation. However, the two simulations represented in Figure 7 do exhibit obvious formation of extended, filamentary structure due to gravitational collapse, as can be seen from the maps of the column (mass) density (indicated by the contours in the left-hand panels of Figure 11 for B10E1 ζ 1 and of Figure 12 for B3E1 ζ 0).

To investigate whether gravity affects the regions close to and far away from these filamentary structures, we have divided the map of velocity centroids into two regions: the *low-density region* where the column density N lies below the mean column density value (which is $N = 1$ in simulation units), and the *high-density region* where N is larger than the mean. We then measured the velocity anisotropy individually for each region, which is accomplished by restricting the disc-sampling method to discs which lie exclusively within the selected region. The results of this investigation are included in Figure 7. For the low-density region (which makes up the larger fraction of the map), the velocity anisotropy behaves similarly to that measured on the whole map; its strength turns out to be somewhat larger than the whole-map result, and its alignment with the POS B -field is maintained very well throughout the simulation. In contrast, the velocity anisotropy measured on the high-density region undergoes a striking development, which is most prominent for the B10E1 ζ 1 simulation (left panels in Fig. 7): it starts out with a strength

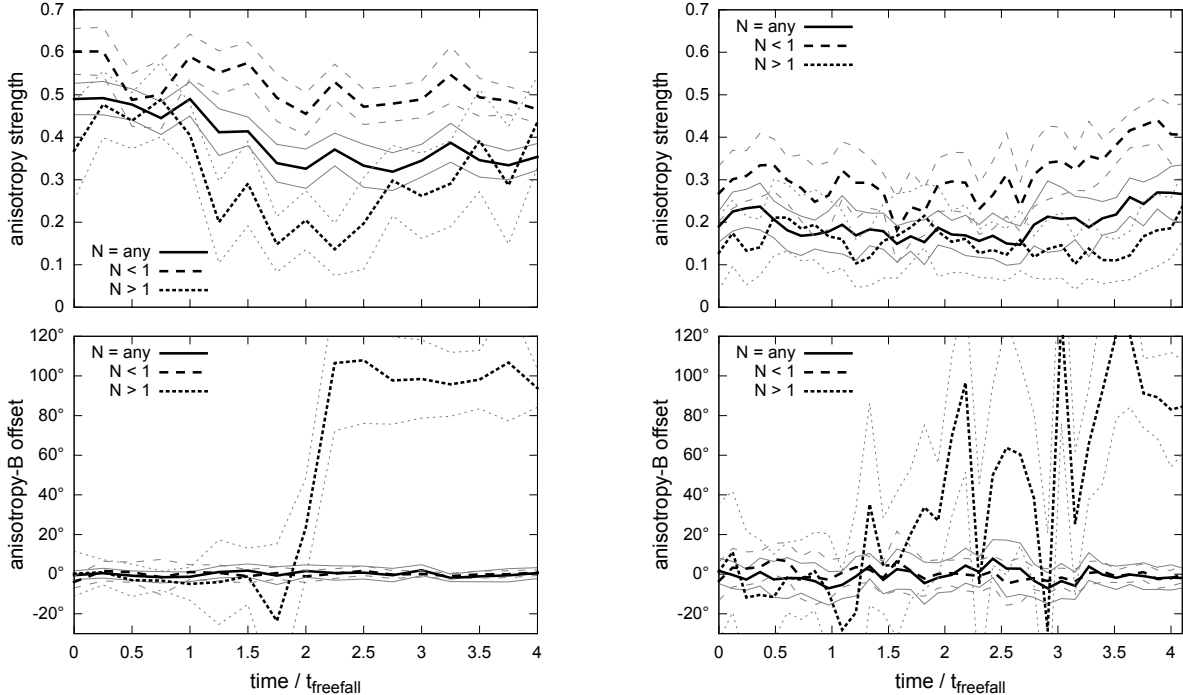


Figure 7. Development of the anisotropy strength (top panels) and of the offset between the anisotropy orientation and the large-scale B -field (bottom panels) over time. The anisotropy was measured at the scale $l = 24$ px. Shown are the results for the B10E1 ζ 1 simulation with $cr = 1$ on the left, and the B3E1 ζ 0 simulation with $cr = 2$ on the right. Thick solid lines show the results from analyzing the complete map, while thick dashed and dotted lines show results from analyzing only regions with column density $N < 1$ and $N > 1$, respectively. The corresponding thin lines indicate the 1σ uncertainties, obtained from the disc-sampling procedure (with $D = 64$ px; see Section 3.2) and from averaging over the two LOS perpendicular to B .

close to that from the low-density region, but then begins to weaken until it reaches almost baseline levels. At that moment, the orientation of the anisotropy loses its alignment with the POS B -field; it instead starts to align in the *perpendicular* direction, though with a larger spread ($\pm 20^\circ$). This re-oriented anisotropy then gathers strength and eventually regains the strength of the initial anisotropy, lying again significantly above the baseline. Qualitatively, a similar behaviour is observed for the B3E1 ζ 0 simulation (right panels in Fig. 7): the velocity anisotropy is initially roughly aligned with the POS B -field, then starts to fluctuate strongly, and eventually settles at an orientation roughly perpendicular to the B -field.

We’d like to stress that the loss and/or change of the velocity anisotropy’s alignment in the high-density regions is indeed caused by gravity, and can not be explained by e.g. shocks which are caused by the turbulence driving. At the moment where we switch on gravity ($t = 0$), the state of the simulation is identical to the preceding pure-MHD stage, and Fig. 7 shows that at $t = 0$ (and in fact for some time thereafter) the velocity anisotropy is well aligned with the POS B -field in all regions, regardless of density. The loss/change of alignment is only encountered after the gravitational collapse has begun

to form structures.

4.3.1. The correlation between velocity anisotropy and local structure

A possible cause for the changing orientation of the velocity anisotropy in the high-density regions is that the velocity field is getting affected by density structures which are emerging due to the gravitational collapse. To investigate this possibility, we focus on the simulation which exhibits this reorientation most prominently (B10E1 ζ 1), and take a look at the pairwise correlations between the local orientations of the velocity anisotropy (V), the column density (N), and the magnetic field (B). Here, the local orientation of the column density is measured by a method analog to that for the velocity anisotropy (i.e. based on the the second order structure function of the column density, cf. Sec. 3), and analysed at the same scale of $l = 24$ px. The results are shown in Fig. 8. On one hand, we observe that in the low-density region (left panel), all three orientations are parallel to each other (with offsets $< 20^\circ$), where the tightest correlation is seen between V and B . Over time, the correlation between all three orientations becomes even stronger. On the other hand, in the high-density region (see Fig. 8, right panel) the three correlations develop

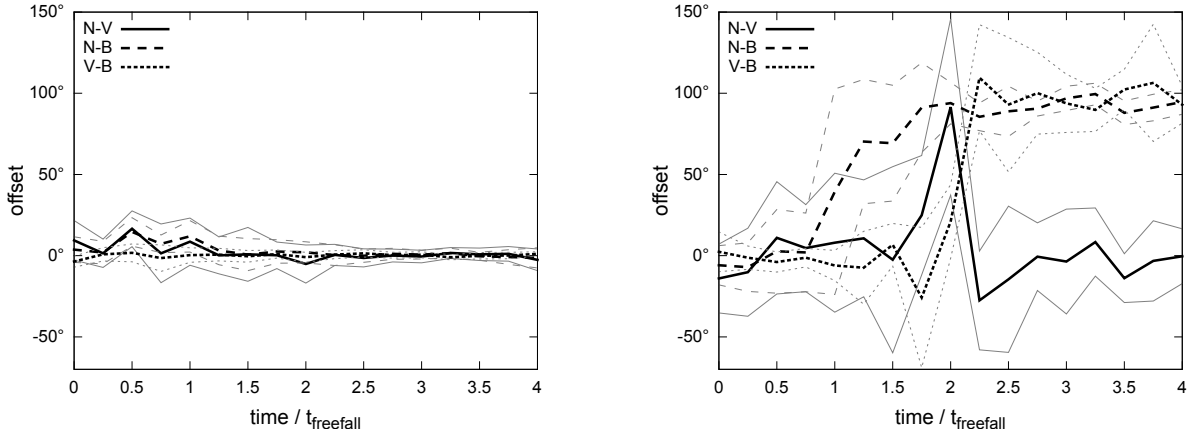


Figure 8. Development of the offset between the local orientations of the column density (N), velocity anisotropy (V), and magnetic field (B), for the B10E1 ζ 1 simulation with $cr = 1$ and starting at the time when self-gravity is switched on. The left and right panels show results for the regions with $N < 1$ and $N > 1$, respectively. The thin lines indicate the 1σ uncertainties as in Fig. 7.

very differently. We observe that first (around $t = 1t_{\text{ff}}$) the offset between N and B (dashed line) switches from parallel to perpendicular, and this correlation becomes quite tight ($\sigma < 10^\circ$) at later times. As noted before, the offset between V and B (dotted line) also switches from parallel to perpendicular, though with some delay compared to the $N - B$ offset. Consequently, the offset between N and V (solid line) switches briefly from parallel to perpendicular, then back again. We note that the correlation between the V orientation and both the B and N orientations is much weaker (with $\sigma \gtrsim 20^\circ$) than that between N and B . This indicates that in this simulation, the local structure formation is governed by the magnetic field. The fact that the velocity anisotropy only changes its orientation after the column density structures perpendicular to the B -field have formed (around $t = 2t_{\text{ff}}$) indicates that indeed it is the presence of these structures which affects the velocity anisotropy orientation.

Focusing on the later stage of the gravitational collapse (at $t = 3t_{\text{ff}}$ for the aforementioned B10E1 ζ 1 simulation), Fig. 9 shows how the pairwise absolute offsets between the local orientations of N , V , and B are distributed on the plane-of-sky. We note again that in the low-density region (i.e. outside the indicated $N = 1$ contour) all three orientations tend to be parallel to each other. The $N - B$ offset (middle panel), switches very sharply from parallel to perpendicular near the transition from low- to high-density region. While the $V - B$ offset (right panel) shows almost exclusive parallelity in the low-density region, it is dominated by perpendicular orientations in the high-density region. The $N - V$ offset presents a more complex pattern, where perpendicular orientations are observed in the transition region between low and high column density, but parallel ori-

entations dominate both the diffuse region outside the cloud and the region deeper inside the cloud. A more quantitative analysis of the relative orientations between N , V , and B inside the high-density region is presented in Fig. 10. The most pronounced feature is seen in the $N - B$ offset, which peaks sharply at $\pm 90^\circ$, indicating a strong tendency for perpendicular orientations. In contrast, the $V - B$ offset shows a rather flat distribution with weak peaks at $\pm 90^\circ$, i.e. a much weaker tendency for perpendicular orientations. Likewise, the $N - V$ offset displays a shallow peak around 0° , which indicates a slight preference for parallel orientations.

In summary, we observe that the gravitational collapse has little influence on the strong correlation between velocity anisotropy and B -field orientation in regions of low column density (they remain parallel), but in higher density regions only relatively weak correlations can be found for the velocity anisotropy. There it tentatively aligns parallel to local density structures and hence perpendicular to the B -field, since the structures are strongly influenced by the B -field and form perpendicular to it. The behavior of the velocity anisotropy is particularly unclear in the transition region between low and high column density (compare Fig. 9), which may obscure its behavior inside the denser region unless the denser region is of significant extent. For the simulation discussed in this section (B10E1 ζ 1, $cr = 1$) this is indeed the case, as the strong B -field ($\mathcal{M}_A \approx 0.24$) leads to the formation of an extended filament on the plane-of-sky. How the velocity anisotropy in the high density region correlates with such large scale structures in general, will be discussed in the next subsection.

4.3.2. The correlation between velocity anisotropy and large-scale structure

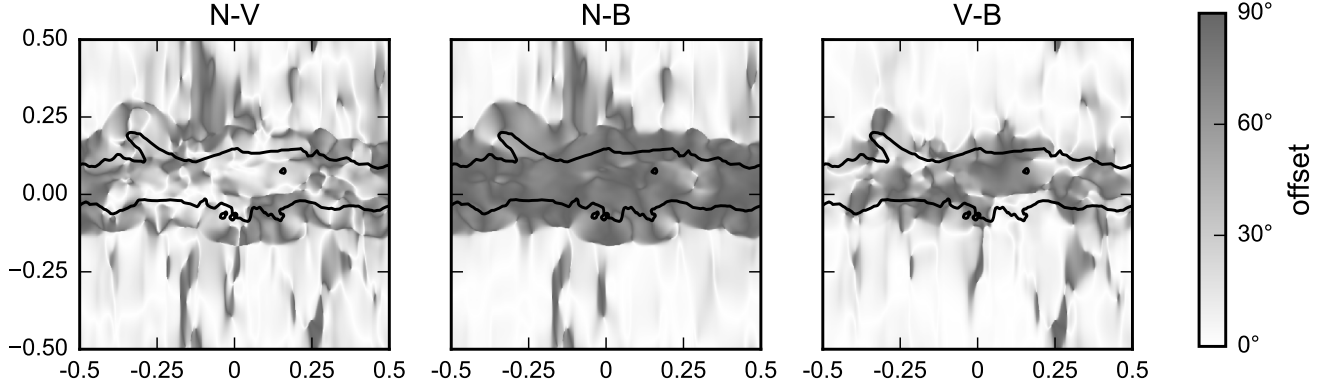


Figure 9. Maps of the absolute offset between the local orientations of the column density (N), the magnetic field (B), and the velocity centroid anisotropy (V), for the B10E1 ζ 1 simulation with $cr = 1$ at $t = 3t_{\text{ff}}$, along the x -LOS. The black contour indicates $N = 1$, i.e. the high-density region is inside this contour while the low-density region is outside. The mean magnetic field points in the vertical direction (z -axis).

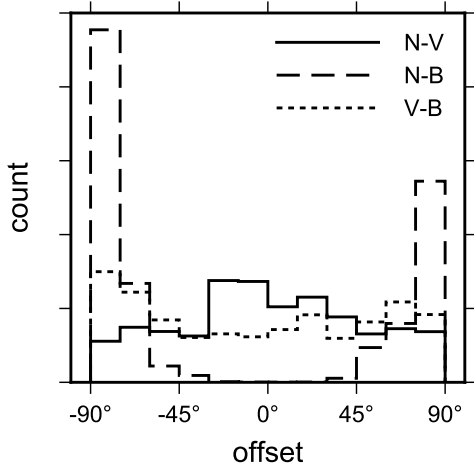


Figure 10. Histograms of local orientation offsets in the high-density region ($N > 1$) for the same snapshot as in Fig. 9. The histogram bins are 15° wide.

The two simulations highlighted in Figure 7 develop large-scale column density structures which lie roughly perpendicular to the POS B -field (lefthand panels of Figures 11 and 12). To better quantify how these structures are oriented, we employ a method based on the autocorrelation of the column density (Li et al. 2013). Taking into account the periodic boundary conditions, we first apply a Fourier transform to the entire column density map, then take its absolute square, then apply an inverse Fourier transform, which yields a map of the column density’s autocorrelation. We then select the contour which surrounds the top 10% of autocorrelation values. Then we determine the principal axes of the area inside this contour; the longer axis is used to define the orientation of the structure, and the aspect ratio (length of longer axis divided by length of shorter axis) can be used to define how strongly the structure is oriented. The righthand panels of Figures 11 and 12 show

the autocorrelation maps with the top-10% contour for the two exemplary simulations B10E1 ζ 1 and B3E1 ζ 0, respectively. For B10E1 ζ 1, we obtain a POS angle of 175° and an aspect ratio of 5.5; for B3E1 ζ 0, the POS angle is 3° and the aspect ratio is 5.1. That is, in both simulations the column density structure is strongly oriented, and aligned close to perpendicular to the mean POS B -field (which has a POS angle of $\approx 90^\circ$).

As was shown in Fig. 7, for the two highlighted simulation runs we find that the velocity anisotropy in the high-density region becomes aligned with the orientation of the forming structure, while in the low-density region the anisotropy stays aligned with the B -field. We remind the reader that the orientation of the velocity anisotropy is defined as that direction in which the dispersion of the line-of-sight velocity centroid is minimal. Looking at the map of the velocity centroid (colormaps in the lefthand panels of Figures 11 and 12), we can get an idea why the anisotropy orients itself differently in the low- and high-density regions. In the low-density region, the velocity centroid map exhibits elongated structures (“striations”) along the z -axis (parallel to the B -field). Moving along a striation, the velocity centroid changes little, but moving across a striation, it changes more rapidly. Hence the velocity centroid dispersion is minimal along the B -field. But in the high-density region, the striations disappear, and there is instead a tendency for the velocity centroid to stay more constant within individual column density contours. Moving along such a contour changes the velocity centroid less strongly than moving across the contours. Hence the velocity centroid dispersion is now minimal along the contour structures, which lie perpendicular to the B -field.

Clearly defined column density structures (where the top-90% column density autocorrelation contour has an

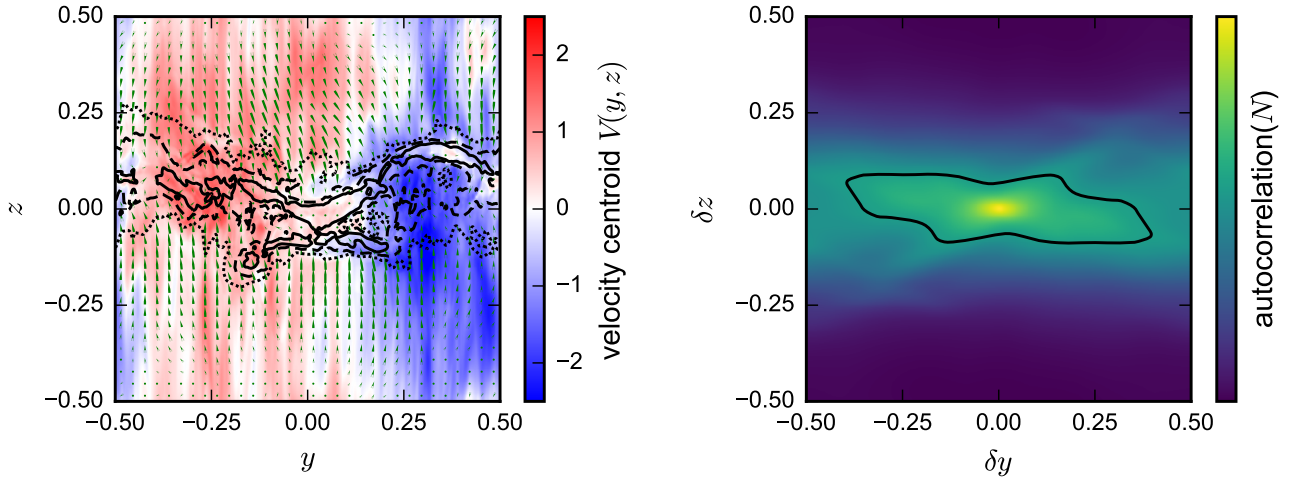


Figure 11. (Color online) *Left:* Map of the velocity centroid (along the x -LOS) for the B10E1 ζ 1 simulation with criticality 1, at $t = 2 t_{\text{ff}}$. The contours indicate column densities at 1x (dotted), 2x (dashed), and 4x (solid) the mean column density. The green arrows show the plane-of-sky velocity field (density-weighted; length proportional to the magnitude). *Right:* Corresponding map of the autocorrelation function of the column density N . The contour surrounds the top 10% of autocorrelation values.

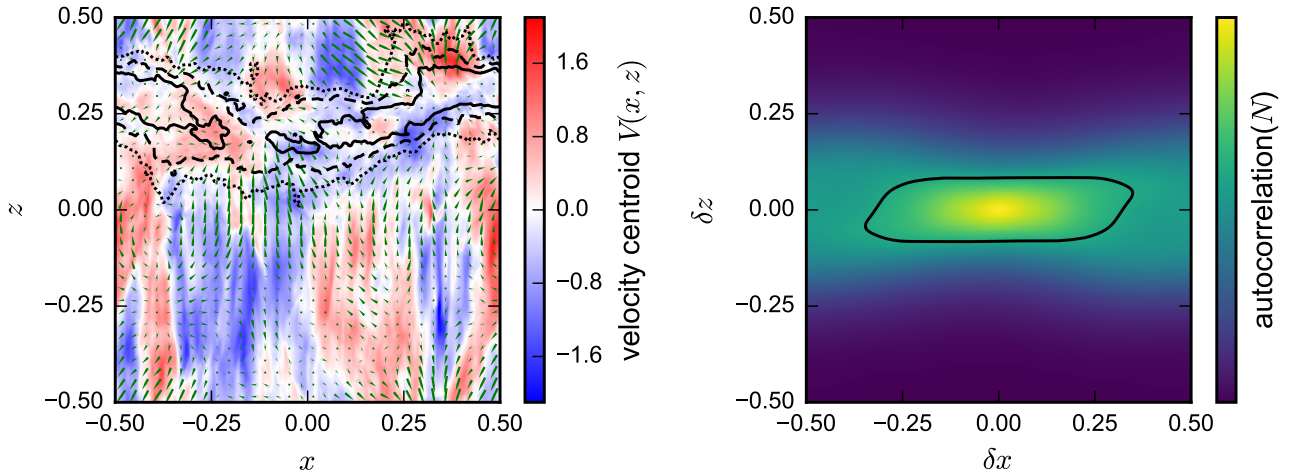


Figure 12. (Color online) Like Fig. 11, but for the B3E1 ζ 0 simulation with criticality 2 at $t = 3.8 t_{\text{ff}}$ and along the y -LOS.

aspect ratio above 4) form not only in the two exemplary simulation runs mentioned above, but in about half (14 of 26) of our simulations with gravity (see Table 1 for details). Figure 13 shows how these structures correlate with the averaged velocity anisotropy in the high-density region. The yellow-colored data points correspond to snapshots from early stages of gravitational collapse, where structures have started to form (lower aspect ratio) perpendicular to the B -field, and the velocity anisotropy has weakened but still tends to be aligned with the B -field, hence having $\approx 90^\circ$ offset from the orientation of the density structure. In the progression from orange over red to purple data points, the structures become more pronounced (increasing aspect ratio) while the velocity anisotropy weakens and starts to deviate from the B -field orientation. The black data points correspond to snapshots from the final stage of

gravitational collapse, where structures are strongly oriented (aspect ratio > 8) and the velocity anisotropy has become aligned parallel to these structures (within 10°) and has gained strength.

In summary, for those simulations where gravitational collapse leads to clearly oriented structures (like filaments), we universally find that the velocity anisotropy in the high-density region becomes preferentially aligned with the structure instead of with the B -field. However, as pointed out in subsection 4.3.1, this correlation is weaker than what is found in the low-density region, where velocity anisotropy strongly aligns parallel to the B -field.

5. DISCUSSION

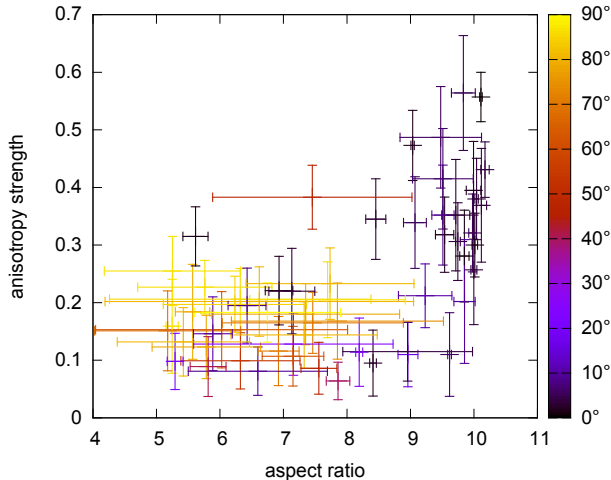


Figure 13. (Color online) Correlation between high-density velocity centroid anisotropy and column density autocorrelation structure. Each data point represents one snapshot from the gravitational stage of one of our simulations. The horizontal axis shows the aspect ratio of the top-10% contour of the column density’s autocorrelation (averaged over the two LOS perpendicular to the B -field). The vertical axis shows the anisotropy strength measured from the velocity centroid in the high-density region, i.e. where column density $N > 1$ (also averaged over the two LOS $\perp \mathbf{B}$). The colour indicates the offset between the orientation of the column density autocorrelation contour and the orientation of the velocity centroid anisotropy. (This plot only includes snapshots where the aspect ratio is larger than 5, to prevent the data from becoming too dense.)

As detailed in Section 1, velocity anisotropy has been studied before by a variety of means, and here we wish to discuss similarities and differences with the results of some of the previous works. Most closely related to the present investigation are the studies from Esquivel & Lazarian (2011) (hereafter EL11) and Burkhart et al. (2014) which also employ velocity centroid data (obtained from MHD simulations of turbulence without self-gravity) to measure the velocity anisotropy. In these studies, the anisotropy strength is measured using the “isotropy degree” which is the ratio of the velocity centroid’s structure function (at a certain scale) in the directions parallel and perpendicular to the POS B -field. These studies did not discuss how the orientation of the anisotropy could be determined, and assumed that it aligns with the POS B -field (at least on small scales). In contrast, our method of fitting the angular dependence of the structure function (at a certain scale) to a simple model function directly measures not only the strength of the anisotropy, but also its orientation. Hence our method is of advantage if one wants to apply it to observational data, where the POS B -field orientation is not necessarily known (or not necessarily with good accuracy).

Regardless of the different anisotropy measure, we con-

firm one of the major findings of EL11, namely that the anisotropy strength depends both on the alfvénic and the sonic Mach number (recall Figure 6 for our results). In general, the anisotropy is most pronounced if both Mach numbers are small. Increasing the alfvénic or the sonic Mach number leads to a decrease of the anisotropy strength, though we find that the anisotropy remains detectable even for highly supersonic ($\mathcal{M} \approx 17$) or mildly super-alfvénic ($\mathcal{M}_A \approx 1.2$) conditions. Likewise, Esquivel & Lazarian (2011) find detectable anisotropy up to $\mathcal{M}_A \approx 1.5$.

Measuring the velocity anisotropy from observational data has been the topic of Heyer et al. (2008) (hereafter H+08) and Heyer & Brunt (2012) (hereafter HB12), with the goal of estimating the magnetic field strength in the Taurus molecular cloud. These studies used a more elaborate method than the one presented here, which applies principal component analysis to PPV spectroscopic data. By calibrating the method against numerical simulations, the strength of the POS B -field component can be inferred. H+08 focused on low-density striations in the envelope of the cloud, and report a well-defined velocity anisotropy which is aligned with the POS B -field. Their PCA-based method yields an estimate of $B_{\text{POS}} = 14 \mu\text{G}$, which coincides well with the estimate from the Chandrasekhar-Fermi method. HB12 extended the study of the Taurus cloud to higher density regions through inclusion of optically thinner ^{13}CO data. Notably, no significant velocity anisotropy was detected in the higher density regions (where visual extinction $A_V > 2$). HB12 propose that the absence of velocity anisotropy in these regions is due to the transition from sub- to super-alfvénic conditions with increasing density, although their major argument for the existence of super-alfvénic turbulence in the high-density regions seems to be the absence of velocity anisotropy. HB12 further suggest that ambipolar diffusion (i.e. the contracting gas decouples from the B -field and leaves the B -field behind) may be responsible for this change of the alfvénic Mach number.

Our study offers an alternative explanation for the observations in HB12. As we saw in Section 4.3, if the gravitational contraction causes the formation of oriented structures (which certainly applies to the filamentary Taurus cloud), then the velocity anisotropy in the high-density region may disappear, or even become aligned with the structure instead of with the B -field. Hence the absence of velocity anisotropy in the $A_V > 2$ ^{13}CO data may simply be caused by gravity, and is not necessarily an indication for super-alfvénic conditions inside the high-density regions.

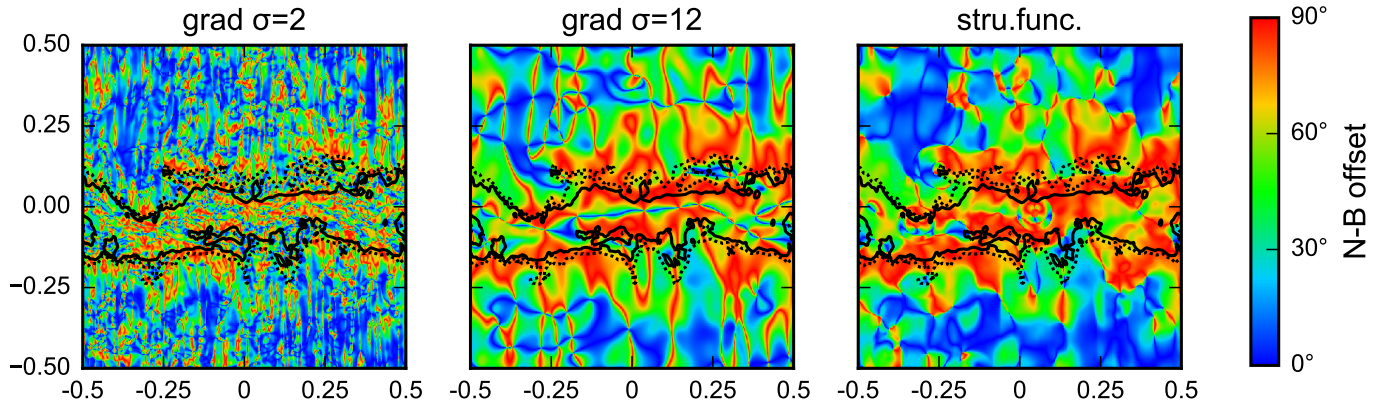


Figure 14. (Color online) Map of the absolute offset between the local orientations of column density (N) and magnetic field (B), for the B10E2 ζ 0 simulation with $cr = 1$ at $t = 4t_{\text{ff}}$, along the x -LOS, where the B -field points in the vertical direction (z -axis). The dotted and solid black contours indicates $N = 1$ and $N = 2$, respectively (in units of mean column density). The three panels show different methods for determining the local N -orientation. In the left panel, the density gradient method is employed, with width $\sigma = 2$ px for the Gaussian derivative kernel (see text); likewise in the middle panel with $\sigma = 12$ px. In the right panel, local N -orientation is determined from the anisotropy of the local structure function of N , at the scale $l = 24$ px. The colour scale has been chosen to allow visual comparison with Fig. 9 from [Planck Collaboration et al. \(2016\)](#).

In fact, we can scale one of our simulations (which were carried out in reduced units, see Section 2) such that the physical parameters match the conditions in the Taurus cloud (as reported in H+08 and HB12) reasonably well. For a discussion about how the dimensional scaling is achieved, see e.g. [Li et al. \(2015b, Section 4.1\)](#). Our simulation B10E2 ζ 0 with $cr = 1$ possesses an alfvénic Mach number of $\mathcal{M}_A \approx 0.37$ before gravity is switched on (cf. Table 1), which is close to the $\mathcal{M}_A \approx 0.5$ reported in H+08. Using an isothermal temperature of $T = 15$ K (from H+08) and choosing the box size as $L = 9.2$ pc (somewhat larger than the 3.5 pc region investigated in HB12), the dimensional scaling yields a mean B -field strength of $14 \mu\text{G}$, matching the estimate from H+08. The total mass inside this scaled simulation is $\sim 3400M_{\odot}$, and the mean column density is $N(\text{H}_2) = 1.94 \cdot 10^{21} \text{ cm}^{-2}$ which corresponds to a visual extinction of $A_V = 1.04$ mag ([Bohlin et al. 1978](#); [Vrba & Rydgren 1984](#)). After $t = 4t_{\text{ff}} = 15.5$ Myr of gravitational collapse, a well-defined filamentary structure has formed in this simulation, which is nearly perpendicular to the mean B -field (offset $91^{\circ} \pm 2^{\circ}$). See the black contours in Fig. 14 for an illustration of this structure. In the low-density region (here using $A_V < 2$ to match HB12), we measure a velocity anisotropy strength $b = 0.59 \pm 0.04$ which is tightly aligned with the B -field (deviation $< 2^{\circ}$). In the high-density region ($A_V > 2$), the anisotropy is much weaker at $b = 0.2 \pm 0.1$ and possesses a very unclear alignment (POS angle $147^{\circ} \pm 48^{\circ}$). This matches HB12’s observation of an inconclusively defined anisotropy in the high-density region. However, as our simulation provides full access to the three-dimensional velocity field, we can evaluate the Mach numbers inside the low- and high-density region. First we note that the

B -field strength doesn’t deviate strongly from the mean value due to the sub-alfvénic setup of this simulation. Thus we obtain $\mathcal{M}_A = 0.56$ in the region with $A_V < 2$ and $\mathcal{M}_A = 0.54$ for $A_V > 2$, for both lines of sight perpendicular to the mean B -field. While the Mach number has increased compared to the initial condition (which is due to energy released by the gravitational collapse), we don’t find an appreciable difference in Mach numbers between the low- and high-density region. Nevertheless, the explanation from HB12 which invokes ambipolar diffusion cannot be ruled out by our simulation, as our numerical method employs ideal MHD and hence does not include ambipolar diffusion effects.

Although the focus of this study has been on the orientation of the velocity anisotropy, we would like to add some final remarks on the relation between the orientations of the B -field and of the density structures. In the simulations presented here, we found large-scale dense structures forming perpendicular to the mean (i.e. large-scale) B -field. In observations of nearby molecular clouds from the Gould Belt, it has been found that the large-scale cloud structure aligns preferentially either perpendicular or parallel to the large-scale (inter-cloud) plane-of-sky B -field, giving rise to a bimodal distribution of the cloud-field alignment ([Li et al. 2013](#)). We’d like to stress that, in the present simulations, we do not encounter this bimodal alignment for the large-scale structures, which may be due to the limited scope and restricted physics model of our simulation setup. However, we do see a bimodal alignment between density structures and B -field on the *local* scale – they tend to be parallel in regions of low column density, but perpendicular for high column density. This matches ob-

servational findings from Gould Belt clouds reported in [Planck Collaboration et al. \(2016\)](#) (hereafter: Planck XXXV). While we determine the orientation of local structures from the anisotropy of the column density’s local structure function at a given scale l , in Planck XXXV the local structure orientation is defined as perpendicular to the gradient of the column density. Computing this gradient using a Gaussian derivative kernel ([Soler et al. 2013](#)) also allows to set the scale at which the local orientation is analyzed (this corresponds to smoothing the column density map with a Gaussian of a certain width σ before taking the gradient). To test whether the differing definitions of local structure orientation influence the conclusion about the local structure-field alignment, we return to the previously discussed B10E2 ζ 0 simulation, since (as argued before) it has comparable properties to the Taurus region, which was also part of the Planck XXXV study. Fig. 14 presents the plane-of-sky distributions of the local structure-field alignment, using the density gradient method with convolution widths $\sigma = 2$ px and $\sigma = 12$ px (left and middle panel, respectively) and our structure function based method with $l = 24$ px (right panel). First, we note that the alignment patterns in the left and middle panel possess strong visual similarity to those in the 10’ and 60’ maps of the Taurus region in Fig. 9 from Planck XXXV. Second, we note that in the middle and right panel, the size and distribution of the patches with parallel (blue) and perpendicular (red) alignment closely match, indicating that these two analysis agree both in the analysed scale and in the result for the local structure orientation.¹ Regardless of the analysis method or scale, we observe that parallel structure-field alignment occurs mostly in the low-density region, while the high-density region is dominated by perpendicular alignment, i.e. the same bimodal distribution of alignment as reported in Planck XXXV. But to reiterate, this bimodal alignment is here seen on the sub-cloud scale and must not be confused with the bimodal alignment seen on the cloud/inter-cloud scale in [Li et al. \(2013\)](#).

6. SUMMARY

Velocity anisotropy is present in synthetic maps of line-of-sight velocity centroid data which we have obtained from numerical simulations of driven magnetohydrodynamics turbulence. The two-point second-order structure function of the velocity centroid proves to be a use-

¹ The density gradient method tends to exhibit artefacts where the column density displays a ridge or a valley, which accounts for the major part of the discrepancies between the middle and right panel of Fig. 14.

ful tool for detecting and quantifying this anisotropy. In the sub- to trans-alfvénic regime which we have investigated here, we reliably find significant velocity anisotropies which are strongly aligned with the plane-of-sky (POS) magnetic field. This holds particularly when the anisotropy is evaluated at scales which are small compared to the turbulence driving scale. Additionally we find that the turbulence driving mechanism (here modelled as either purely solenoidal or purely compressive) has a minor to insignificant influence on the quantitative results for the velocity anisotropy. Hence the method employed here may be used to infer the orientation of the POS magnetic field from velocity data, coming e.g. from spectroscopic observations.

When self-gravity is neglected, we find that the strength of the velocity anisotropy depends on both the sonic and the alfvénic Mach number (\mathcal{M} and \mathcal{M}_A , respectively), in good agreement with [Esquivel & Lazarian \(2011\)](#). Hence a determination of the anisotropy strength is not sufficient to determine \mathcal{M}_A , even if the B -field is known to lie on the plane-of-sky. However, when other observations or constraints for \mathcal{M} (e.g. from non-thermal linewidths) and for B_{LOS} (e.g. from Zeeman observations) are available, it is possible to infer additional constraints for \mathcal{M}_A through the velocity anisotropy.

When self-gravity is taken into account, we find that significant velocity anisotropy is still present in regions of lower column density, where it remains aligned with the POS B -field. In contrast, in regions of higher column density, the velocity anisotropy may disappear, or there might even develop an anisotropy which is aligned not parallel to the POS B -field, but parallel to the density structures which emerge from the gravitational collapse. This holds particularly if these structures are of extended size and exhibit clear directional preference, like e.g. filaments.

This result provides an explanation for the loss of velocity anisotropy which has been observed in high-density regions of the Taurus molecular cloud ([Heyer & Brunt 2012](#)). It has been proposed that this loss is caused by the transition to super-alfvénic conditions inside the high-density region, but in our simulation (with parameters matching the Taurus cloud) we find that the alfvénic Mach number in the low- and high-density regions is the same, $\mathcal{M}_A \approx 0.55$. Nevertheless this simulation also exhibits the observed loss of velocity anisotropy in the high-density region. Hence we conclude that this loss is not necessarily associated with a transition to super-alfvénic conditions.

We expect that our method for investigating the velocity

anisotropy can be applied to observational velocity data in a fairly straightforward manner. While projection effects certainly need to be taken into account, [Burkhart et al. \(2014\)](#) have shown that they do not preclude the anisotropy from being detected in velocity centroid data. Another possible caveat is determining a good column density threshold for separating the low- from the high-density region, as the velocity anisotropy may behave differently in these regions. The simple criterium of using the mean column density, as used for our simulation data, can not directly be applied to observations, since the mean column density changes when the studied region is shrunk or enlarged. We plan to investigate this issue and apply our method to observational data in a future work.

This research was supported by the Hong Kong Research Grants Council, project ECS 24300314; and by the CUHK Direct Grant for Research Project 4053073 and 4053126. WJ gratefully acknowledges financial support from the Hong Kong Research Grants Council Collaborative Research Fund “Research in Fundamental Physics: from the Large Hadron Collider to the Universe”.

APPENDIX

A. TURBULENCE DRIVING SCHEME

In our simulations, turbulence is driven by periodically exciting random velocity perturbations in Fourier space. This follows the scheme set forth in [\(Stone et al. 1998\)](#). When a certain period dt_{drv} of simulation time has passed, we set up a field of velocity perturbations $\mathbf{a}(\mathbf{k})$, where \mathbf{k} is the wave vector in Fourier space, such that each component $a_i(\mathbf{k})$ is normally distributed with mean zero and variance $\propto k^6 \exp(-8k/k_{\text{drv}})$. This ensures that the orientations of the vectors $\mathbf{a}(\mathbf{k})$ are isotropically distributed, and that the perturbation power spectrum (accounting for the degeneracy in k) follows

$$k^2 |\mathbf{a}(\mathbf{k})|^2 \propto k^8 \exp(-8k/k_{\text{drv}}) . \quad (\text{A1})$$

This power spectrum is sharply peaked around $k = k_{\text{drv}}$, hence the spatial driving scale is given by L/k_{drv} , where L is the box length of the simulation domain.

Following [\(Schmidt et al. 2006\)](#), to allow for a controlled mix between solenoidal and compressive components in the perturbing field, we apply a \mathbf{k} -dependent projection

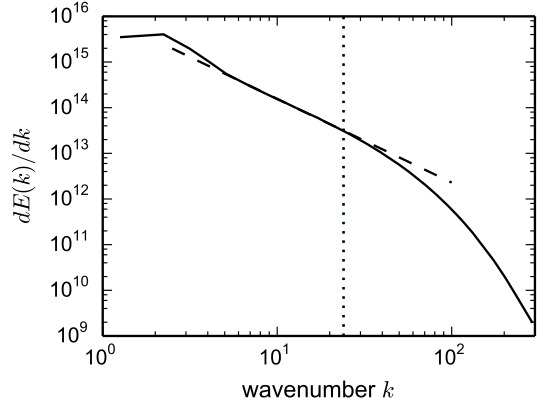


Figure A1. Turbulent power spectrum of the B0E1z1 simulation. The dashed line shows a fit to the spectrum inside the inertial range ($5 \lesssim k \lesssim 25$), extended for better visibility. The dotted line at $k = 24$ indicates the spatial scale $l = N/k = 24$ px, where $N = 576$ px is the number of grid points per dimension.

matrix $\underline{\underline{P}}(\mathbf{k})$ to the generated field $\mathbf{a}(\mathbf{k})$:

$$\delta \tilde{\mathbf{v}}(\mathbf{k}) = \underline{\underline{P}}(\mathbf{k}) \mathbf{a}(\mathbf{k}) \quad (\text{A2})$$

$$P_{ij}(\mathbf{k}) = \zeta \delta_{ij} + (1 - 2\zeta) k_i k_j / |\mathbf{k}|^2 \quad (\text{A3})$$

The parameter $\zeta \in [0, 1]$ determines the fraction of solenoidal components. For $\zeta = 1$, the driving field is purely solenoidal (divergence-free, non-compressive), which can be pictured as turbulence driven by stirring motions. On the other hand, for $\zeta = 0$, the driving field is purely compressive (curl-free), which can be pictured as turbulence driven by compressing or dilating motions (e.g. shock waves).

Each component $\delta \tilde{v}_i(\mathbf{k})$ is then multiplied with a uniformly random complex phase (under the provision that $\delta \mathbf{v}(-\mathbf{k}) = \delta \mathbf{v}(\mathbf{k})^*$ to ensure that its Fourier transform is real-valued), which avoids spatially static patterns in the driving field. The Fourier-transformed velocity perturbations $\delta \mathbf{v}(\mathbf{x})$ are then shifted such that no net momentum will be added to the simulation domain, and normalized such that the increase in total kinetic energy will match a prescribed parameter value, dE_{drv} . In effect, the turbulent energy input ratio, $dE_{\text{drv}}/dt_{\text{drv}}$, will be constant over time.

The turbulent power spectrum is given by $dE(k)/dk$, where $E(k)$ is the total specific kinetic energy at scales with wavenumbers up to k , i.e. $E(k) = \int_{|\mathbf{k}'| \leq k} d^3 \mathbf{k}' \tilde{\mathbf{v}}(\mathbf{k}')^2$. For the B0E1z1 simulation, this power spectrum is shown in Fig. A1; here the spectrum was averaged over a series of ten snapshots of fully developed turbulence. As our employed MHD code is based on finite differencing, it is rather diffusive, so that the turbulent inertial range is not well developed; it spans the range $5 \lesssim k \lesssim 25$. In Section 4 some analyses are

carried out at “small” spatial scales; we chose to employ the scale $l = 24$ px for this which, as Fig. A1 shows, still

lies inside the inertial range and is hence unaffected by numerical dissipation effects.

REFERENCES

- Bohlin, R. C., Savage, B. D., & Drake, J. F. 1978, *ApJ*, 224, 132
 Burkhart, B., Lazarian, A., Leão, I. C., de Medeiros, J. R., & Esquivel, A. 2014, *ApJ*, 790, 130
 Cho, J., & Lazarian, A. 2003, *MNRAS*, 345, 325
 Cho, J., Lazarian, A., & Vishniac, E. T. 2002, *ApJ*, 564, 291
 Cho, J., & Vishniac, E. T. 2000, *ApJ*, 539, 273
 Esquivel, A., & Lazarian, A. 2005, *ApJ*, 631, 320
 —. 2011, *ApJ*, 740, 117
 Esquivel, A., Lazarian, A., & Pogosyan, D. 2015, *ApJ*, 814, 77
 Esquivel, A., Lazarian, A., Pogosyan, D., & Cho, J. 2003, *MNRAS*, 342, 325
 Federrath, C., Roman-Duval, J., Klessen, R. S., Schmidt, W., & Mac Low, M.-M. 2010, *A&A*, 512, 81
 Goldreich, P., & Sridhar, S. 1995, *ApJ*, 438, 763
 Hayes, J. C., Norman, M. L., Fiedler, R. A., et al. 2006, *ApJS*, 165, 188
 Heyer, M., Gong, H., Ostriker, E., & Brunt, C. 2008, *ApJ*, 680, 420
 Heyer, M. H., & Brunt, C. M. 2012, *MNRAS*, 420, 1562
 Lazarian, A. 2004, *JKAS*, 37, 563
 Lazarian, A., & Pogosyan, D. 2000, *ApJ*, 537, 720
 Li, H.-b., Dowell, C. D., Goodman, A., Hildebrand, R., & Novak, G. 2009, *ApJ*, 704, 891
 Li, H.-b., Fang, M., Henning, T., & Kainulainen, J. 2013, *MNRAS*, 436, 3707
 Li, H.-B., Goodman, A., Sridharan, T. K., et al. 2014, *Protostars and Planets VI*, 101
 Li, H.-B., Yuen, K. H., Otto, F., et al. 2015a, *Natur*, 520, 518
 Li, P. S., McKee, C. F., & Klein, R. I. 2015b, *MNRAS*, 452, 2500
 McKee, C. F., & Ostriker, E. C. 2007, *ARA&A*, 45, 565
 Nakano, T., & Nakamura, T. 1978, *PASJ*, 30, 671
 Planck Collaboration, Ade, P. A. R., Aghanim, N., et al. 2016, *A&A*, 586, A138
 Rosolowsky, E. W., Goodman, A. A., Wilner, D. J., & Williams, J. P. 1999, *ApJ*, 524, 887
 Schmidt, W., Hillebrandt, W., & Niemeyer, J. C. 2006, *CF*, 35, 353
 Soler, J. D., Hennebelle, P., Martin, P. G., et al. 2013, *ApJ*, 774, 128
 Stone, J. M., Ostriker, E. C., & Gammie, C. F. 1998, *The Astrophysical Journal Letters*, 508, L99
 Vrba, F. J., & Rydgren, A. E. 1984, *ApJ*, 283, 123